ACS APPLIED NANO MATERIALS

www.acsanm.org Article

Transparent Porous ZnO|Metal Complex Nanostructured Materials: Application to Electrocatalytic CO_2 Reduction

Julian Guerrero, Nathanaelle Schneider, Fabienne Dumoulin, Daniel Lincot, Umit Isci,* Negar Naghavi,* and Marc Robert*

Cite This: *ACS Appl. Nano Mater.* 2023, 6, 10626−10635 Read Online

ACCESS | Metrics & More | Article Recommendations | Supporting Information

ABSTRACT: We developed a simple and versatile approach for the electrochemical growth of hybrid ZnO|molecular catalyst nanostructured layers. Metal oxide|catalyst hybrid nanoporous layers with a sponge-like structure at the nanoscale and multiscale three-dimensional (3D) hierarchical structures based on nanoporous zinc oxide (ZnO) layers grown on ZnO nanorods were obtained. The thickness and structure of the hybrid nanoporous layers as well as the catalyst concentration can be tuned. This method allows the introduction of water-soluble molecular catalysts based on porphyrin and/or phthalocyanine derivatives into the ZnO matrix with a homogeneous distribution of the complex into the material. As an illustrative example, combining hybrid ZnO with a very low concentration of an encapsulated Co-based molecular catalyst inside the oxide layer results in a 97% catalytic response toward CO_2 reduction to CO with large currents in an organic solvent, highlighting the excellent electrocatalytic activities of such layers, which combine porosity, electronic conductivity, and synergetic properties from its components.

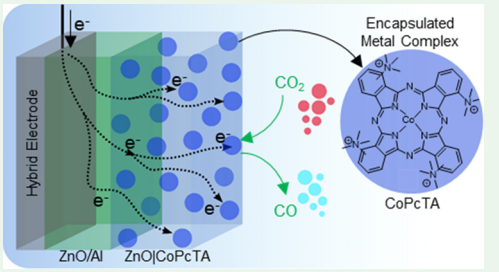

KEYWORDS: *hybrid material, nanomaterials, molecular catalyst, cobalt complex, electrochemical CO_2 reduction*

INTRODUCTION

Inorganic−organic hybrid materials are a class of compounds gaining more and more interest due to their distinct chemical and physical properties.[1] They are disordered physical−chemical systems in which inorganic components (metal ions, oxides, sulfides, nonmetallic elements, etc.) and organic components (organic molecules, ligands, biomolecules, polymers, etc.) are brought together by specific interactions, resulting in a synergistic enhancement of their functional properties[2] and functional capabilities that would not be possible with just one of the components. This emerging field of research has already found a broad range of applications such as energy storage, high-performance capacitors, solar cells, catalysis, and photocatalysis.[3,4] Besides, electrocatalytic reactions, such as the reduction of CO_2 (CO_2RR), are an appealing option for storing renewable electricity and producing valuable chemicals and fuels such as CO, HCOOH, CH_4, CH_3OH, and CH_3CH_2OH[5] in a sustainable manner. CO_2RR not only is a thermodynamically uphill process but also suffers from slow kinetics. Moreover, poor catalytic selectivity and high overpotential continue to limit efficiency and upscaling of CO_2 electroreduction.[6] The search for increased activity, selectivity, and stability of catalysts requires the development of new systems. The combination of organic and inorganic hybrid nanostructured materials may play a significant role toward these aims. While using nanostructured or high surface area catalysts can significantly improve surface reactivity by making a significant fraction of the reactive sites available for catalysis, the use of organic−inorganic hybrid materials can open up the possibility of addressing new properties of catalysts that would otherwise be inaccessible using purely organic or inorganic materials.

Currently, a variety of earth-abundant metal-based molecular catalysts have been identified, reporting high selectivity for the CO_2 reduction reaction.[5,7−9] Among examples, cobalt phthalocyanine has been identified as a good electrocatalyst for CO_2RR owing to its high selectivity and activity for CO production.[10,11] Besides, oxide-derived metal-based materials such as CuO, Cu_2O,[12−15] Ag_2O,[16,17] NiO,[18,19] and TiO_2[20−22] have been successfully demonstrated to be active and selective catalysts for CO_2 reduction. ZnO, a low toxic compound, is an oxide-derived non-noble metal with promising optical,[23] electronic,[24] photovoltaic,[25−27] and catalytic properties.[28−31] Recently, a maximum faradaic efficiency (FE) of 92% for CO_2 to CO conversion has been reported for a nanoporous (NP) ZnO.[32] However, the catalytic system suffered from degradation issues due to morphological changes during CO_2 reduction in aqueous media.

Received: April 10, 2023
Accepted: May 29, 2023
Published: June 12, 2023

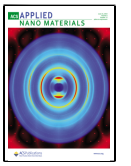

https://doi.org/10.1021/acsanm.3c01591
ACS Appl. Nano Mater. 2023, 6, 10626−10635

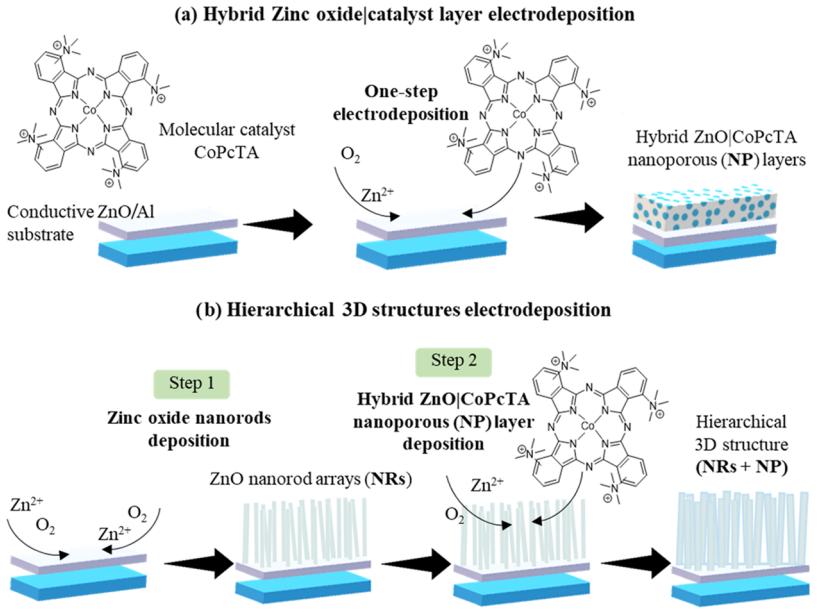

Figure 1. Schematic representation of the preparation of the ZnO nanostructures. (a) Hybrid **ZnO|CoPcTA** nanoporous (**NP**) layers and (b) hierarchical 3D structures made of zinc oxide nanorod arrays (**ZnO NRs**) coated by a hybrid ZnO|catalyst nanoporous (**NP**) layer (**ZnO NRs + ZnO|CoPcTA NP**).

ZnO has the distinct advantage of being easily prepared in high quality and in a wide range of nanostructures, such as nanorods,[33,34] nanotubes,[35,36] and nanobelts,[37,38] via solution routes such as chemical bath deposition (CBD)/dip coating,[39] chemical vapor deposition (CVD)/spray pyrolysis,[40] hydrothermal synthesis,[41] and electrochemical deposition.[42,43] Electrodeposition is a low-temperature (mostly <100 °C) cost-effective deposition process that allows the design of complex ZnO nanostructures by combining and adjusting the growth conditions.[33,34,44,45] In the late 1990s, Yoshida and coworkers[46] described one-step electrodeposition of nanostructured ZnO/organic films onto conducting substrates for photovoltaic applications, by adding water-soluble dyes such as tetrasulfonated metallophthalocyanines to the electrochemical bath containing $Zn(NO_3)_2$. The loading of organic molecules into ZnO films was also attempted using a $ZnCl_2$ bath employing cathodic reduction of the dissolved molecular oxygen precursor.[45,47,48] In the present study, electrodeposited ZnO layers will be used as a matrix for the incorporation of molecular catalysts.

Incorporation of molecular catalysts onto the surfaces of electrodes can be achieved in a variety of manners. Typically, grafting methods are used where the catalyst's ligand structure is chemically modified with appropriate anchoring groups that allow surface binding through either a noncovalent or covalent mode. Polymer binders can also be used to immobilize catalysts on the surface of electrodes.[49] However, immobilized catalysts on the electrodes' surface must remain stable for long periods of time under catalytic operating conditions. In addition, immobilization should not affect the catalytic activity of the complex. Developing nanostructure organic−inorganic hybrid catalysts in which a metal oxide can act as a porous cage that grows around the molecular catalyst, allowing the diffusion of substrate and product molecules in and out of the catalytic material, not only could prevent the catalyst from leaching out, but it may also provide large electrochemical surface areas and increase CO_2 adsorption capacity around the active sites, resulting in excellent efficiency and long-term stability in CO_2 reduction. However, to the best of our knowledge, very limited reports have exclusively focused on implementing this strategy in the electrochemical reduction of CO_2.

Herein, we present the preparation of molecular metal complex-modified nanostructured ZnO thin-film electrodes, focusing on the attractive ability to tune their chemical, optical, electrical, and catalytic properties upon altering the film composition and thickness. The strength of the proposed method lies in its one-step electrodeposition route to produce a nanoporous or nanostructured oxide matrix while simultaneously encapsulating the catalyst. Two different nanostructured electrodes with self-supported catalyst hybrid layers were developed. First, **CoPcTA**, a water-soluble tetracationic Co phthalocyanine complex, was employed as an encapsulated molecular catalyst within a transparent and conductive ZnO nanoporous matrix. Following a two-step deposition process, the aforementioned hybrid layers were deposited on ZnO nanorods, resulting in three-dimensional (3D) ZnO hierarchical structures (Figure 1). Finally, replacing **CoPcTA** with other water-soluble molecular catalysts such as tetrasulfonated cobalt phorphyrin (**CoTSPP**) or a tetrasulfonated nickel phthalocyanine (**NiTSPc**) was investigated, illustrating the versatility of the preparation method, which could be used for the incorporation of a wide range of molecular complexes containing various metals and ligands. A combination of analytical, UV−vis, inductively coupled plasma (ICP), X-ray photoelectron spectroscopy (XPS), attenuated total reflection-infrared (ATR-IR), grazing incidence X-ray diffraction (GIXRD), and energy-dispersive X-ray spectroscopy (EDX) mapping techniques was used to confirm the incorporation and potential synergy between metal−organic catalysts and the oxide matrix. Linear/cyclic voltammetry (CV) and controlled potential electrolysis (CPE) experiments confirmed the accessibility and catalytic activity of the hybrid organic−inorganic layers. Material characterization and redox behavior have been investigated, demonstrating homogeneous dispersion and control of molecular metal complex loading through the oxide matrix. These hybrid electrodes were tested as

https://doi.org/10.1021/acsanm.3c01591
ACS Appl. Nano Mater. 2023, 6, 10626−10635

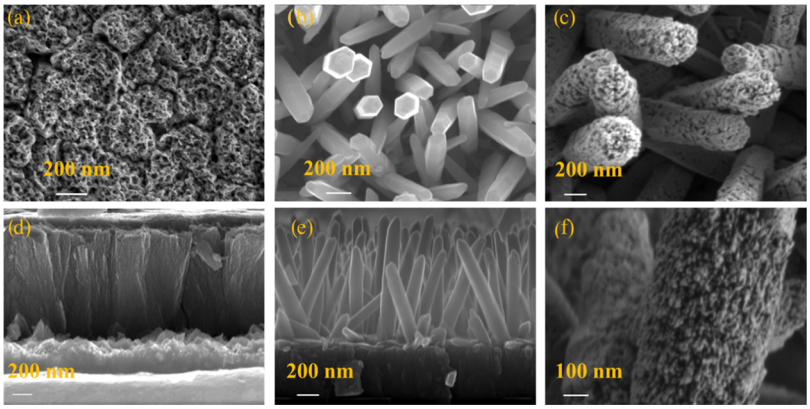

Figure 2. Top view and cross section scanning electron microscope (SEM) images of the different ZnO nanostructures presented in this work: (a, d) **ZnO|CoPcTA NP**, (b, e) **ZnO NRs**, and (c, f) **ZnO NRs** covered by a thin **ZnO|CoPcTA NP** layer.

cathode materials in electrocatalysis. Taking CO_2 reduction as an illustrative example, their remarkable potential was demonstrated.

RESULTS AND DISCUSSION

Hybrid Electrodes' Preparation and Characterization. In this work, electrodeposited ZnO was first used as a matrix for incorporation of **CoPcTA**, a water-soluble molecular cobalt phthalocyanine catalyst. A glass covered with 350 nm of a ZnO:Al layer deposited by atomic layer deposition (ALD) was used as a substrate. The procedure to prepare the nanostructured electrodes is schematically shown in Figure 1, along with microscopic characterization data (Figure 2). Two nanostructured layers have been developed and combined with a molecular catalyst: a nanoporous **ZnO|CoPcTA** structure (NP; Figure 1a) and a 3D hierarchical structure made of 20 nm of the nanoporous **ZnO|CoPcTA** structure (NP) grown on zinc oxide nanorods (ZNRs; Figure 1b).

The electrodeposition of the **ZnO|CoPcTA NP** hybrid layers was carried out at a constant potential in an aqueous oxygen-saturated solution containing $ZnCl_2$, KCl salts, and **CoPcTA** (see the Methods section for details). Figure 3 compares the X-ray diffraction patterns under the grazing incidence (GIXRD) of the ALD ZnO:Al substrate with those of a **ZnO|CoPcTA NP** layer, pure **ZnO NRs**, and a hybrid 3D structure of **ZnO NRs** covered by a ~20 nm **ZnO|CoPcTA NP** layer. For all layers, the diffraction patterns match the standard diffraction patterns of the hexagonal wurtzite ZnO crystal structure (JCPDS-36-1451).[50] The ALD ZnO:Al substrate (Figure 3a) presents a mixed (100), (101), and (110) orientation, indicating that the *c*-axis of ZnO is mostly parallel to the substrate. As observed in the SEM images (Figure 2a,d), addition of the molecular catalyst during the growth of ZnO seems to strongly affect the crystal growth mechanism of ZnO, leading to a significantly higher surface area, resulting in a sponge-like nanoporous structure. The comparison of the X-ray diffraction patterns of the **ZnO|CoPcTA** nanoporous layer with the ALD ZnO:Al substrate shows an increased peak intensity of the (002) planes for the nanoporous layer as well as the appearance of (102) and (103) reflections (Figure 3c). The nanoporous film is thus mainly oriented according to the (002) reflection, which corresponds to the *c*-axis of the wurtzite-type lattice. Such preferential orientation is often observed for ZnO layers, as the (002) crystal face is the densest and the most stable thermodynamically.

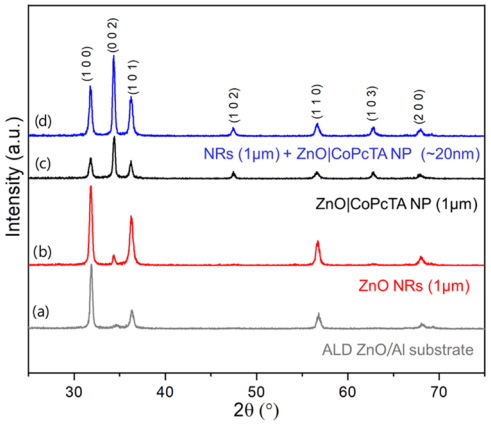

Figure 3. GIXRD patterns under grazing incidence for (a) ALD ZnO:Al substrate, (b) **ZnO NRs** (1 μm) grown on the ALD ZnO:Al substrate, (c) **ZnO|CoPcTA NP** layer grown on the ALD ZnO:Al substrate, and (d) **ZnO NRs** covered by the **ZnO|CoPcTA NP** layer (NRs + NP).

When **ZnO NRs** are grown on the ALD ZnO:Al substrate, it results in nonvertical randomly oriented rods as observed in SEM images (Figure 2b,e) while presenting the same crystalline orientation and diffraction planes as the ALD ZnO:Al substrate (Figure 3b). Interestingly when the **ZnO|CoPcTA NP** layer is grown on **ZnO NRs** (Figure 3d), the same preference orientation occurs as with the **ZnO|CoPcTA NP** layer for which the most intense peak remains (002). This confirms that when **CoPcTA** is added to the deposition bath, whatever the substrate orientation, nanoporous layers tend to self-organize with a preferential *c*-axis orientation along the (002) plane. For these layers, SEM pictures show a hierarchical structure composed of a hybrid **ZnO|CoPcTA NP** coat surrounding the nanorods (Figure 2c,f). Effective covering of **ZnO NRs** arrays with **ZnO|CoPcTA NP** layers has been achieved by varying the total charge transferred during the electrodeposition (Figure S1).

The thickness of the **ZnO|CoPcTA NP** layer can be controlled by varying the transferred charge throughout the process. Increasing the charge from 0.5 to 4 C cm^{-2} results in a linear increase in NP layer thickness from 20 to 1200 nm (Figure S2). It has been shown that adding a water-soluble molecular complex to the ZnO electrodeposition bath can not

https://doi.org/10.1021/acsanm.3c01591
ACS Appl. Nano Mater. 2023, 6, 10626−10635

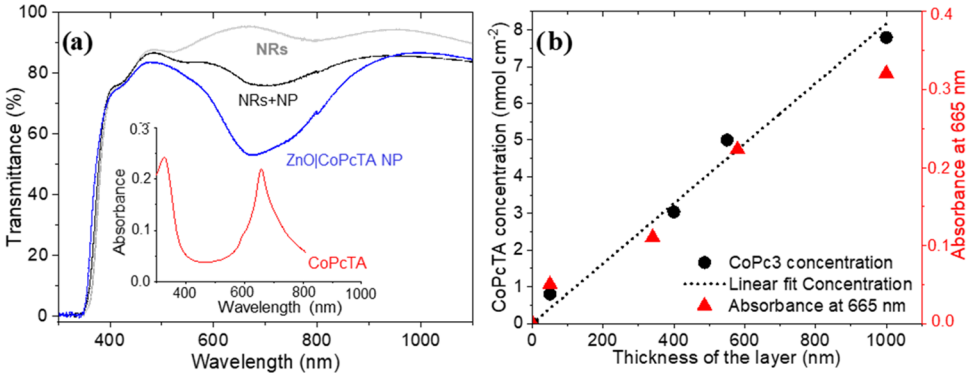

Figure 4. (a) Optical transmission of electrodeposited **ZnO NRs** (1 μm, gray), **ZnO|CoPcTA NP** layer (1 μm, blue), and 3D ZnO **NRs** (1 μm) coated by **ZnO|CoPcTA NP** (20 nm, black) on ALD ZnO:Al. Inset: absorbance of the **CoPcTA** molecule in aqueous solution (concentration = 50 μM, red). (b) Concentration of **CoPcTA** molecules in the **ZnO NP** layers measured by ICP as a function of the thickness of the layer and comparison to the absorbance of the same samples at λ = 665 nm.

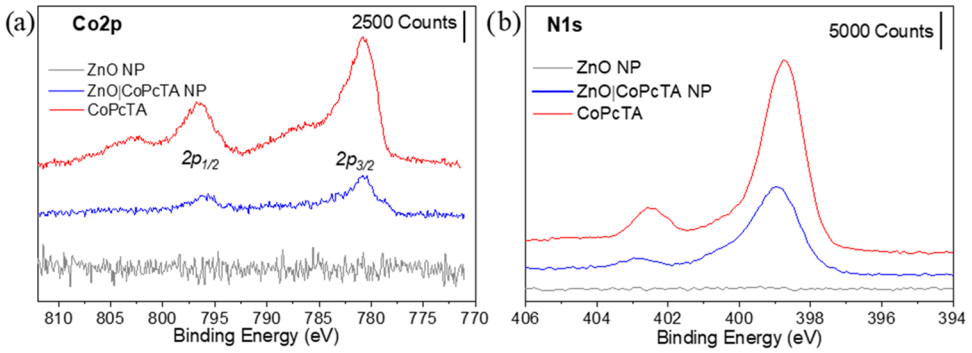

Figure 5. Comparison of the XPS core level spectra of (a) Co 2p and (b) N 1s for the **CoPcTA** molecule, the **ZnO|CoPcTA NP** electrode, and a blank ZnO electrode.

only act as a structure-directing agent but also result in its incorporation inside the nanoporous ZnO layer.[44,47] Inductively coupled plasma optical emission spectrometry (ICP-OES) and optical absorption measurements on **ZnO|CoPcTA NP** samples were performed to confirm the incorporation of the molecular catalyst into the electrodeposited layers (Figure S3). The results of ICP measurements are presented in Figure 4b, showing that after dissolution of the layers (acidic treatment with water-diluted nitric acid), catalyst loadings range from 0.8 ± 0.2 nmol cm^{-2} for a 50 nm thick **ZnO|CoPcTA NP** layer up to 7.8 ± 0.7 nmol cm^{-2} for a 1 μm thick **ZnO|CoPcTA NP** layer. The concentration of the **CoPcTA** molecule inside the layers is linearly correlated to the film thickness. Furthermore, the optical absorbance measurements show that the **ZnO|CoPcTA NP** samples present an absorbance peak at around 665 nm in a wavelength range, which is close to the absorbance peak of the **CoPcTA** molecule in aqueous solution (Figure 4a). A linear relationship is observed between the layer thickness and the **CoPcTA** concentration inside the layer (Figure S4), as well as between the layer thickness and the absorbance at 665 nm (Figure 4b). This strongly suggests the molecule's incorporation into the hybrid layers, the amounts of which can be adjusted by controlling the deposition time (i.e., the charge being transferred).

Moreover, ICP analysis was performed on 3D **ZnO NRs** (1 μm) covered with 20 nm of the **ZnO|CoPcTA NP** layer. In these layers, the ICP analysis shows a **CoPcTA** concentration of around 0.73 nmol cm^{-2}, which corresponds to approximately 10 times less than the one measured for a 1 μm thick **ZnO|CoPcTA NP** layer.

Figure 4a compares the optical transmission of electrodeposited **ZnO NRs** (1 μm), **ZnO|CoPcTA NP** layer (1 μm), and 3D **ZnO NRs** (1 μm) coated by a **ZnO|CoPcTA NP** (20 nm) layer on the ALD ZnO:Al substrate and the absorbance of an aqueous solution of the pure **CoPcTA** molecule (50 μM). In the visible range, the transparency of **ZnO NRs** approaches 90%. The impact on the total transmission of the incorporation of the **CoPcTA** molecule into the nanoporous **ZnO|CoPcTA NP** layers becomes clear between 525 and 1000 nm, with a decrease from ∼97% transmission to ∼55% (580−700 nm range) for a 1 μm thick **ZnO|CoPcTA NP** layer. Such a decrease originates from Co complex incorporation, with **CoPcTA** presenting an absorption peak around 665 nm. Optical transmission is significantly improved (>75%) upon using hierarchical structure **ZnO NRs + NP** thanks to the very low amount of the catalyst incorporated in the structure.

Dispersion and distribution of the catalyst into the nanoporous layers were also investigated by EDX mapping measurement. Images from a 1 μm thick **ZnO|CoPcTA NP** electrode (Figure S5) show not only signals from the O, Zn, and Cl atoms of the ZnO matrix but also signals from Co, definitively confirming the catalyst incorporation into the film during the electrodeposition. Additionally, the mapping of the Co element reveals the absence of cobalt aggregates, suggesting a homogeneous distribution of the catalyst in the oxide material.

https://doi.org/10.1021/acsanm.3c01591
ACS Appl. Nano Mater. 2023, 6, 10626−10635

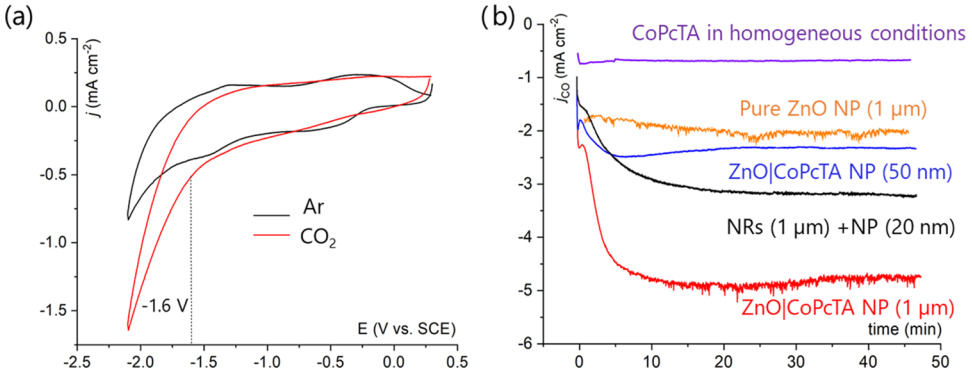

Figure 6. (a) Cyclic voltammograms recorded in Ar (black) and CO_2 (red) saturated acetonitrile solution + 0.1 M $TBAPF_6$ at a 1 μm thick **ZnO|CoPcTA NP** electrode. Electrode surface: 0.5 cm^2 and scan rate: 0.1 V s^{-1}. (b) CPE at $E = -2.1$ V versus SCE in a CO_2-saturated acetonitrile solution + 0.1 M $TBAPF_6$ and 0.67 M H_2O for **CoPcTA** (0.5 mM) in homogeneous conditions (purple), a 1 μm thick ZnO porous layer without a catalyst (orange), a 50 ± 10 nm thick **ZnO|CoPcTA NP** layer (blue), a 1 μm thick **ZnO NRs** covered by a 20 nm thick **ZnO|CoPcTA NP** (**NRs + NP**) layer (black), and a 1000 ± 70 nm thick **ZnO|CoPcTA NP** layer (red).

XPS measurements were performed to assess the presence of the **CoPcTA** molecule and its eventual interaction with the electrodeposited ZnO matrix. The Co 2p and N 1s signals obtained for **CoPcTA**, **ZnO|CoPcTA NP**, and a blank ZnO layer with no molecular complex are compared in Figure 5. From **ZnO|CoPcTA NP**, two peaks corresponding to Co 2p signals indicative of a Co^{2+} oxidation state are observed (Figure 5a), with a main peak ($2p_{3/2}$) at 780 eV and a secondary peak at ($2p_{1/2}$) at 796 eV.[51] In Figure 5b, signals from nitrogen are also detected on the surface of the **ZnO|CoPcTA NP** electrodes, with the N 1s signal peak at 398.8 eV, a similar value to the characteristic binding energy of isoindolic N in phthalocyanines complexing a cobalt atom (BE = 399.3 eV).[51] This peak reflects the configuration of the CoN_4 center with four equivalent nitrogen atoms coordinating a Co^{2+} ion. Furthermore, a small additional N 1s peak centered at 402.5 eV is observed, which is typically assigned to N−O bonds,[52] indicative of a possible interaction between the N atoms of the **CoPcTA** molecule and the oxygen atoms of the sample holder (Si wafer covered by native oxide). All these results clearly confirm that **CoPcTA** is incorporated into the hybrid **ZnO|CoPcTA NP** layers. In order to have a better understanding of the interactions between the molecular catalyst and the inorganic ZnO matrix, the O 1s and Zn 2p XPS spectra of **ZnO|CoPcTA NP** layers were compared to those of the blank ZnO layers (Figure S6). The peaks do not show any shift in the binding energy value before and after the incorporation of the molecular catalyst. However, further analysis must be done in the future to probe for the possible interactions between the molecule and the ZnO inorganic matrix.

The infrared spectroscopy analysis (ATR-IR) of **CoPcTA**, a 1 μm **ZnO|CoPcTA NP** sample, and a ZnO blank sample was also compared (Figure S7). The analysis data reveal similar fingerprint regions between **CoPcTA** powder and **CoPcTA** loaded into the **ZnO|CoPcTA NP** layer, which further evidences that the catalyst is well entrapped into the ZnO-electrodeposited layer. The metal-to-ligand (M−N) vibration of **CoPcTA** could be observed at 910 cm^{-1}, as well as peaks around 1080 cm^{-1} (C−N stretching bending vibrations) and at 1393 cm^{-1}. These latter peaks are assigned to aromatic ring stretching vibrations, showing a perfect match with the vibration obtained with a **CoPcTA** powder sample. The peaks from the CH_3 groups at 2895 and 2986 cm^{-1} indicate structural preservation of the organic molecule upon incorporation into the ZnO inorganic matrix.[53]

Electrochemical CO_2 Reduction by ZnO|Catalyst Hybrid Nanostructures. The catalytic activity of the **ZnO|CoPcTA NP** electrodes was first explored by cyclic voltammetry (CV) in an acetonitrile solution containing 0.6 M H_2O and 0.1 M tetrabutylammonium hexafluorophosphate ($TBAPF_6$). A catalytic current with an onset potential of ca. −1.6 V versus SCE is observed when the solution is saturated with CO_2 (Figure 6a). Addition of H_2O as a proton source (0.33 M, 0.44 M, and 0.67 M) was investigated. As observed in the cyclic voltammograms (Figure S8a), the H_2O concentration increase results in an enhancement of the current density and in a decrease of the overpotential of ca. 200 mV upon going from 0.33 to 0.67 M H_2O. Adding more water (>0.7 M) does not show a significant impact on the current density but accelerates the degradation of the electrodes. Furthermore, increasing the thickness of the NP layers allows them to reach higher current densities, as quantified by CVs of 50, 530, and 1000 nm thick **ZnO|CoPcTA NP** layers, of ca. 0.5, 1.4, and 2.0 mA cm^{-2}, respectively (Figure S8b). The increase of the current density with the thickness of the NP layer suggests that the current density depends on the active surface area of the electrodes as well as on the amount of the catalyst inserted into the layers. Thanks to the nanoporous structure of the electrodes, the reactant CO_2 can access the active sites even in a 1 μm thick layer.

This was confirmed upon performing CPE experiments. A comparison of electrodes covered with **ZnO|CoPcTA NP** layers of 50 ± 10, 530 ± 50, and 1000 ± 70 nm thicknesses (Figure S9) shows a current density increase with the thickness of the **NP** layer. Even with a 1 μm thick layer, the **CoPcTA** molecules incorporated into the ZnO nanoporous matrix are accessible and can react with CO_2, and the overall electrocatalytic process is only partially limited by diffusion of the reactant and charge transport through the oxide film. Moreover, these results add further evidence that the **CoPcTA** catalyst is well dispersed and distributed throughout the thickness of the layer and not just on the surface. The electrodes show good stability for 45 min of CPE. During the first 10 min, the current gradually increased until it reached a steady-state value staying stable until the end of the experiment. This behavior may be due to the porosity of our layers, since it takes some time for the reactant (CO_2) to fill

https://doi.org/10.1021/acsanm.3c01591
ACS Appl. Nano Mater. 2023, 6, 10626−10635

Table 1. Comparative Data of the Performance of the Different ZnO Nanostructure Catalytic Materials during a 45 min Electrolysis Experiment at a Constant Potential E of − 2.1 V versus SCE in a CO_2-Saturated Acetonitrile Solution Containing 0.1 M $TBAPF_6$ and 0.67 M H_2O[a]

					selectivity			
entry	sample	catalyst amount	current density (mA cm^{-2})	total FE (%)	%CO	%H_2	TON	TOF (s^{-1})
1	**CoPcTA** in homogeneous solution	0.5 mM	− 0.45	98.1	60.8	39.2	0.93	0.001
2	1000 nm blank ZnO nanoporous layer	0	− 2.04	99.0	73.7	26.3		
3	**ZnO|CoPcTA NP** 50 ± 10 nm	0.81 nmol	− 2.45	98.6	97.4	2.6	17,885	9.4
4	**ZnO|CoPcTA NP** 500 ± 50 nm	1.86 nmol	− 3.37	99.6	98.4	1.6	9283	4.9
5	**ZnO|CoPcTA NP** 1000 ± 70 nm	2.80 nmol	− 5.0	97.1	98.9	1.1	8280	4.4
6	ZnO **NRs** 1 μm	0	− 0.9	98.0	73.5	26.5		
7	ZnO **NRs** 1 μm + ZnO|**CoPcTA NP** 20 nm	0.75 nmol	− 2.9	91.0	96.7	3.3	22,242	11.7

[a]Electrode surface = 1 cm^2.

and reach all of the porosity of the layer; in addition, a similar time effect may also impact the progressive charging of the film (charge transport to the catalytic sites).

CPE experiments at E = −2.1 V versus SCE (45 min duration) were performed with all electrode structures and are compared in Figure 6b. First, the **CoPcTA** molecule in homogeneous conditions shows a weak catalytic activity with a current density of −0.45 mA cm^{-2}, while gas chromatography (GC) analysis of the products indicates the formation of CO with 60.8% selectivity (Table 1, entry 1). A ZnO nanoporous layer can reduce CO_2 to CO with 73.7% selectivity at j = −2 mA cm^{-2} (Table 1, entry 2), i.e., a partial current density for CO production j_{CO} = −1.5 mA cm^{-2}, confirming the catalytic activity of ZnO itself to reduce CO_2 to CO, as reported previously.[29,32,53−58] When both components **CoPcTA** complex and ZnO are combined in a hybrid material, significant enhancement of the CO_2 reduction reaction is obtained. CPE experiments using **ZnO|CoPcTA NP** layers typically lead to current densities ranging from −2.45 to −5 mA cm^{-2} (i.e., ranging from j_{CO} = −2.4 mA cm^{-2} to j_{CO} = −4.95 mA cm^{-2}) when layer thickness increases from 50 to 1000 nm, respectively, while producing CO with selectivity above 97% (Table 1, entries 3−5). The presence of a small amount of **CoPcTA** in the layers not only induces a significant increase in the current density but also strongly improves the selectivity of the reaction. These results illustrate the synergetic effect of the cobalt complexes and zinc oxide for boosting the catalysis, possibly occurring from the joint coordination of CO_2 molecules at the cobalt sites along with assistance from the zinc ions (Lewis acid sites), which provide stabilization of the partial negative charge developing on the oxygen atoms of CO_2 and weakening of the C−O bonds, which is favorable to cleavage. Remarkably, a turnover number (TON) as high as 17,885 and a turnover frequency (TOF) of 9.4 s^{-1} were obtained for the thin (50 nm) NP layer (Table 1, entry 3), standing among the highest performance so far obtained for an immobilized metal complex electrocatalyst.[6,10,59] The TOF value slightly decreases when the thickness of the layer increases (Table 1, compare entries 3, 4, and 5), meaning that overall faster catalysis occurs in a thin layer than that in a thick layer, which may be due to the progressive growing influence of charge transport and diffusional effect limitation in the thicker layers, even if the current density increases across the series of electrodes.

A comparison of CPE experiments of an electrode with a 50 nm **ZnO|CoPcTA NP** thin layer (Figure 6b, blue) with a 3D nanostructured electrode (**NRs** (1 μm) covered by a **ZnO| CoPcTA NP** layer (20 nm); Figure 6b, black line), both incorporating a similar amount of the molecular catalyst (0.81 nmol cm^{-2} and 0.75 nmol cm^{-2}, respectively), shows an enhancement of the catalytic performance toward the CO_2RR for the 3D structure. The partial current density j_{CO} for CO production reached by the NP thin layer is ca. −2.45 mA cm^{-2}, whereas the 3D structured electrode achieves an absolutely higher (j_{CO} = −2.9 mA cm^{-2}) current density (Table 1, compare entries 3 and 7). The 3D structured electrodes also furnish a higher TOF of 11.7 s^{-1}, meaning that the CO production goes faster in the 3D nanostructured electrodes. The combination of good electronic transport properties and the highly exposed surface of the **ZnO NRs** with the catalytic hybrid layer results in an enhancement of the catalytic performance toward the CO_2RR.

We investigated the stability of the electrodes upon performing long-term CPE at −2.1 V versus SCE (2 h) using two samples of 750 ± 50 nm thick **ZnO|CoPcTA NP** layers (Figure 7). An average catalytic current of 3.5 mA cm^{-2} was obtained. Gas chromatography analysis of the products indicates the formation of CO with ca. 97% FE along with H_2 as the only byproduct (3%), giving a complete faradaic efficiency. The current density, after reaching a steady-state value in the first 5 min, remains stable along the electrolysis with a progressive decay. XPS analysis of the electrode before and after the 2 h CPE experiment confirmed electrode stability even if the intensity of the cobalt and nitrogen signals was slightly dampened (Figure S10a,b). We further performed an ICP analysis of the electrode before and after 2 h of

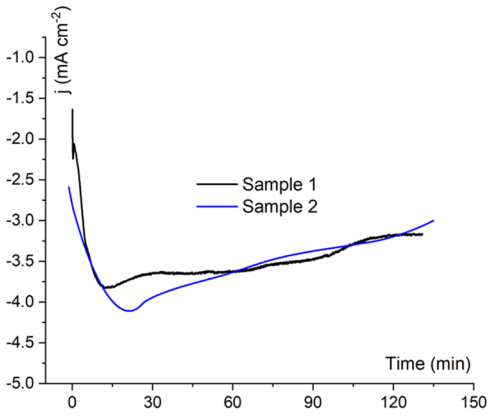

Figure 7. CPE at E = −2.1 V versus SCE in CO_2-saturated acetonitrile solution + 0.1 M $TBAPF_6$ and 0.67 M H_2O for two 750 ± 50 nm **ZnO|CoPcTA NP** layer electrodes.

https://doi.org/10.1021/acsanm.3c01591
ACS Appl. Nano Mater. 2023, 6, 10626−10635

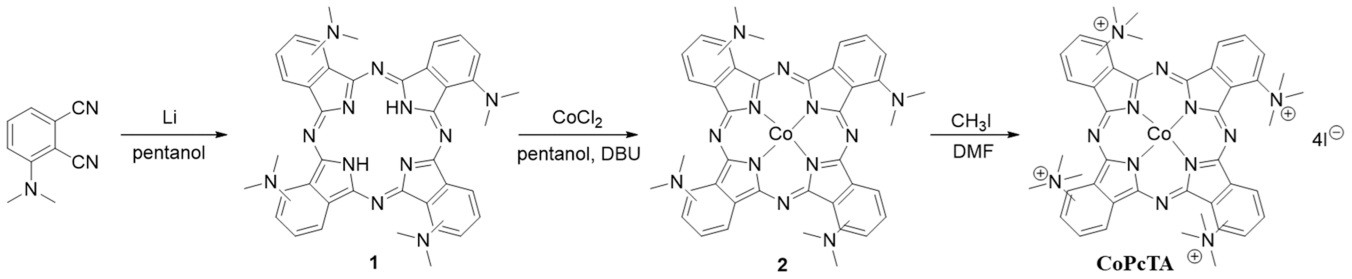

Figure 8. Synthetic route for **CoPcTA**.

electrolysis, revealing a 10% loss of the catalyst from the electrode to the solution. This decrease may reflect the partial cathodic reduction of ZnO into metallic Zn, which could further lead to some catalyst leak. To verify this hypothesis, thorough XPS analyses were performed to characterize the surface properties of the samples before and after CPE. Due to the comparable binding energies of Zn and ZnO in the Zn 2p region of the XPS spectrum, we compared the Zn LMM Auger peaks of the as-prepared and used **ZnO|CoPcTA NP** samples. As shown in Figure S10c, both samples exhibit the typical Auger peaks of ZnO, with a main peak at ∼499 eV and a shoulder at ∼496 eV. Notably, no Zn peaks are present after CPE. However, XRD measurements of the **ZnO|CoPcTA NP** sample after CPE (Figure S10d) show the presence of diffraction peaks from Zn at 2θ = 43.1 and 54.2° corresponding to the (101) and (102) lattice planes of the hexagonal phase from the Zn metal, respectively,[60] indicating that a fraction of the oxidized Zn species is reduced to metallic Zn during electrolysis. Part of the layer may thus have been dissolved, which could explain the loss of the catalyst. Overall, the above results indicate that the **ZnO|Catalyst** films are quite stable with catalytic activity being sustained for hours.

In addition to **ZnO|CoPcTA NP** layers, a porphyrin cobalt complex (**CoTSPP**) and a nickel phthalocyanine complex (**NiTSPc**), both bearing four sulphonated groups, were used to grow ZnO nanoporous layers **ZnO|CoTSPP NP** and **ZnO|NiTSPc NP**. CPE experiments were performed with these electrodes of similar thickness and compared with those investigated before. Total current densities of −1.85, −1.75, and −1.70 mA cm^{-2} were, respectively, obtained for **ZnO|CoPcTA NP**, **ZnO|CoTSPP**, and **ZnO|NiTSPc NP** electrodes (Figure S12). They showed very similar selectivity for CO production, namely, 93.3, 96.9, and 96.8%, respectively (Table S1).

The electroreduction of CO_2 exemplified in the above described examples illustrates the versatility of the preparation method that could be used for the incorporation of a variety of molecular complexes with different metals and ligands with a systematic positive impact of the metal oxide matrix, thus opening a wide range of possibilities for performing various electrocatalytic reactions.

CONCLUSIONS

Hybrid ZnO|catalyst films have been electrodeposited on transparent conductive electrodes by a simple one-step method. The grown nanostructured oxide layers are highly porous and can be loaded with water-soluble metal (e.g., Co, Ni) complexes during the electrodeposition process. Both the thickness (from a few tens of nanometers to a micrometer) and nanostructuration (2D and 3D hierarchical structures) of the oxide layers can be controlled, as well as the quantity of encapsulated molecular complexes, which appear to be homogeneously dispersed in the films. These films are electrochemically active thanks to their high porosity and conductivity. Such modified electrodes may be used for various applications in electrochemical devices. As an illustrative example, selective and fast electroreduction of CO_2 to CO has been achieved, showing a synergetic effect between the molecular catalyst and the zinc oxide hosting matrix. Such an approach could now be applied to other electrocatalytic processes. Remarkably, these electrodes also present significant visible light transmission, which may enable their use as a front contact in photovoltaic and photocatalytic devices. This opens up a modular approach where photoabsorbers and molecular catalysts can be developed, tested, optimized, and exchanged independently.

METHODS

Catalyst Synthesis. Reagents were purchased from Aldrich and used without further purification. 3-(Dimethylamino)phthalonitrile was synthesized according to the literature[10] (see the Catalyst Synthesis Characterization in the Supporting Information). Tetrasulfonated cobalt porphyrin **CoTSPP** and tetrasulfonated nickel phthalocyanine **NiTSPc** were purchased from Aldrich.

Synthesis of Phthalocyanine ***1***. Granules of lithium were added to anhydrous *n*-pentanol (10 mL). This mixture was heated to 60 °C under argon flux until the total consumption of the granules. 3-(Dimethylamino)phthalonitrile (0.5 g, 2.92 mmol) was added and this reaction mixture was refluxed for 18 h. It was then cooled to room temperature and poured into an ethanol/water mixture. The resulting precipitate was filtered off, washed several times with water, and dried. Phthalocyanine **1** (Figure 8) was obtained by chromatography on silica gel using a mixture of CH_2Cl_2/EtOH (20:1) as the eluent. Yield: 35% (175 mg). FT-IR (ν, cm^{-1}): 3290, 3073, 2944, 2832, 2775, 1576, 1485, 1433, 1321, 1186, 1135, 1083, 1035, 970, 879, 804, 745, 667. ^{1}H NMR (500 MHz, DMSO-d_6): δ, ppm, 3.64 (m, 24H), 7.45−8.10 (m, 8H), 8.87 (m, 4H). ESI-HRMS: m/z 687.33840 $[M]^+$ calculated for $C_{40}H_{38}N_{12}$: 686.8280. UV−vis (DMSO): λ_{max} nm (log ε) 342 (4.70), 712 (4.78), 779 (4.89).

Synthesis of Phthalocyanine ***2***. Phthalocyanine **1** (165 mg, 0.24 mmol), $CoCl_2$ (72 mg, 0.48 mmol), and DBU (1 mL) in dried *n*-pentanol (10 mL) were heated to reflux for 18 h under argon. After cooling to room temperature, the reaction mixture was poured into an ethanol/water mixture. The resulting precipitate was filtered off and washed several times with water. Phthalocyanine **2** was purified by chromatography on silica gel using a mixture of CH_2Cl_2/EtOH (10:1) as the eluent. Yield: 70% (125 mg). FT-IR (ν, cm^{-1}): 3069, 2926, 2827, 2775, 1571, 1490, 1438, 1316, 1186, 1156, 1126, 1091, 1052, 987, 914, 870, 805, 740. ESI-HRMS: m/z 744.2588 $[M]^+$ calculated for $C_{40}H_{36}CoN_{12}$: 743.7452. UV−vis (DMSO): λ_{max} nm (log ε) 331 (4.57), 733 (4.68).

Synthesis of Phthalocyanine ***CoPcTA***. Phthalocyanine **2** (150 mg, 0.20 mmol) was dissolved in DMF (10 mL), and methyl iodide (0.9 mL, 15 mmol) was added. The mixture was stirred at 45 °C for 16 h and then poured into diethyl ether (25 mL). The resulting precipitate was filtered off and washed with ether and hexane. Yield: 90% (145

https://doi.org/10.1021/acsanm.3c01591
ACS Appl. Nano Mater. 2023, 6, 10626−10635

mg). FT-IR (ν, cm^{-1}) 3056, 3013, 2952, 2874, 2835, 2784, 1610, 1519, 1481, 1399, 1316, 1270, 1117, 996, 944, 805, 745. ESI-HRMS: m/z 804.3805 $[M + H]^+$ calculated for $C_{44}H_{48}CoN_{12}$: 803.8852. UV−vis (DMSO): λ_{max} nm ($\log \varepsilon$) 330 (4.20), 702 (4.23).

Caution/important note: in order to destroy the excess of methyl iodide, the ether filtrate is treated with triethylamine.

Substrate Preparation. Glass substrates (2 mm thick) covered by a 380 nm thick transparent conductive zinc oxide aluminum-doped (ZnO:Al) layer were used as working electrodes for all of the depositions. This ZnO:Al layer was deposited by atomic layer deposition (ALD) according to the reported procedure (sheet resistance from 20.1 to 28.2 × 10^{-3} Ω sq^{-1}).[61] The ZnO:Al-coated glass substrates were ultrasonically and sequentially cleaned with acetone, 2-propanol, and water, each for 5 min. They were activated in a KOH solution (pH 10.5) for 2 min and finally rinsed with distilled water prior to electrodeposition.

Preparation of the Hybrid Nanoporous Catalytic Layers (ZnO|cat NP). All oxide layers were electrodeposited using a classical three-electrode setup. The reference electrode was a saturated calomel electrode (SCE; Hach) with a potential of +0.244 V versus NHE at 25 °C. The counter electrode was a platinum wire and the working electrodes were the mentioned ZnO:Al-coated glass substrates. The electrodeposition of the zinc oxide|catalyst nanoporous hybrid layers was carried out at a constant potential E of −1.0 V versus SCE in an aqueous solution containing 5.0 mM $ZnCl_2$ (Sigma-Aldrich > 99.9%), 0.1 M KCl (ACS Reagent 99.0−100%), and 50 μM water-soluble catalyst (cobalt phthalocyanine **CoPcTA**, tetrasulfonated cobalt porphyrin **CoTSPP**, or tetrasulfonated nickel phthalocyanine **NiTSPc**). Oxygen gas was bubbled for 20 min prior to the deposition and the same gas flow was maintained during the whole deposition process. The temperature was maintained at 70 °C. The thickness of the layers was controlled from a few tens of nanometers to a micrometer by varying the transferred charge. The deposited films were rinsed with water, dried in air at 100 °C for 30 min, and then stored at room temperature.

Preparation of the 3D Hierarchical Catalytic Structures (ZnO NR + ZnO|cat NP). ZnO nanowire films were first prepared by electrodeposition on an ALD ZnO:Al substrate, according to a method reported elsewhere.[33,34] The ZnO nanowire array layer (**ZnO NR**) was grown at 80 °C from a 0.2 mM $ZnCl_2$ and 0.1 M KCl solution saturated with O_2 by bubbling. The deposition process was stopped when the total transferred charge was 10 C cm^{-2}. The deposited films were rinsed with water and dried in air at 100 °C. These electrodes were then used for the deposition of the metal oxide| catalyst hybrid layers performed as described above, leading to a structure composed of zinc oxide nanorods surrounded by a nanoporous metal oxide/catalyst layer.

Electrochemical Experiments. Linear/cyclic voltammetry measurements and controlled potential electrolysis (CPE) were performed using a PARSTAT 4000A potentiostat (Princeton Applied Research). The electrolyte was an acetonitrile solution with 0.1 M tetrabutylammonium hexafluorophosphate ($TBAPF_6$, 98%, Aldrich), and it was saturated with argon or CO_2 depending on the experiment. Electrodes with hybrid catalytic layers were connected with a clip protected by poly(tetrafluoroethylene) (PTFE) tape, and the electrical contact was ensured by using gallium−indium eutectic (Sigma-Aldrich > 99.9%) covered with copper tape. Copper was isolated from the electrolyte by the PTFE tape leaving an exposed surface of 0.5 cm^2. The abovementioned reference electrode (SCE) was immersed in the same electrolyte in a separate compartment and positioned as close as possible to the working electrode. The counter electrode (platinum wire or mesh) was immersed in the same electrolyte but separated by a glass frit bridge.

The gases used were bought from Air Liquide. Electrolysis using CO_2 as the substrate was performed under 1 atm of the gas, resulting in a concentration of 314 ± 6 mM at 25 °C.[62] Electrolysis experiments were performed in a sealed cell. CPE was typically repeated three times, with a maximum variation of 10% in current density values.

Products Analysis. Gas chromatography analyses of the gases produced during electrolysis were performed with an Agilent Technologies 7820A GC system equipped with a thermal conductivity detector (TCD). CO and H_2 production was quantitatively detected and separated with a CP-CarboPlot P7 capillary column (27.46 m in length and 25 μm in internal diameter). The temperature was held to 150 °C for the detector and 34 °C for the oven. The carrier gas was argon flowing at 9.5 mL min^{-1} at a constant pressure of 0.5 bar. The injections were performed with a 250 μL gas-tight (Hamilton) syringe. These conditions allowed simultaneous detection of H_2, O_2, N_2, CO, CO_2, and CH_4. Calibration curves were determined separately by injecting known quantities of pure gas. From product quantification, TON and TOF were calculated using eqs 1 and 2, respectively.

$$\mathrm{TON} = \frac{n_{\mathrm{product}}}{n_{\mathrm{catalyst\ in\ the\ film}}} \quad (1)$$

$$\mathrm{TOF} = \frac{\mathrm{TON}}{t} \quad (2)$$

Since the electrolysis experiments shown were not conducted until the total deactivation of the catalyst, the given TON value could only be regarded as a lower estimation of the actual value. The amount of the electrochemically active molecular catalyst could be an order of magnitude smaller than the amount of the catalyst present at the electrode. It might also lead to an underestimated value of the calculated TON.[63] Calculations of TON and TOF were made considering the total amount of the molecular catalyst added to the catalyst material. Because the amount of the active catalyst in the film tended to decay over time, the TOF value was an apparent, averaged estimation.

Material Characterization. Thin-film structural properties were determined by X-ray diffraction under grazing incidence (GIXRD) conditions for crystallinity determination and phase detection with a PANalytical Empyrean using Cu Kα radiation. Thin-film morphologies were obtained using a Merlin VP Compact scanning electron microscope (SEM) provided by Zeiss, equipped with an energy-dispersive X-ray spectroscopy (EDS) detector from Bruker. Transmittance and absorbance spectra were obtained using an Agilent Cary 5000 UV−vis−NIR spectrophotometer equipped with an Agilent diffuse reflectance accessory. X-ray photoelectron spectroscopy (XPS) analyses were performed with a THERMO-VG ESCALAB 250 (RX Al Kα excitation at 1486.6 eV). Inductively coupled plasma (ICP) analyses were performed for the determination of the cobalt catalyst concentration in the films. The prepared thin layers were dissolved from the electrode using an acid solution of 69% HNO_3. The resulting solution was then diluted to 2% HNO_3 and injected into an ICAP 6300 Thermo Electron apparatus with the detection of cobalt (238.8 nm).

Chemical Characterization. The NMR spectrum was recorded in DMSO-d_6 on a Varian 500 MHz spectrometer. Infrared spectra (FT-IR) were recorded on a Bio-Rad FTS 175C FT-IR spectrophotometer. UV−visible absorption spectra were obtained using a Shimadzu 2001 UV spectrophotometer. High-resolution mass spectra were measured on an Agilent 6530 Accurate-Mass Q-TOF LC/MS spectrometer equipped with an electrospray ionization (ESI) source.

■ ASSOCIATED CONTENT

Supporting Information

The Supporting Information is available free of charge at https://pubs.acs.org/doi/10.1021/acsanm.3c01591.

Complementary characterization of ZnO layers (SEM, UV−vis, EDX, XPS, AT-IR); cyclic voltammetry and CPE experiments; characterization of catalytic electrodes before and after electrolysis (XPS, Zn LMM Auger spectra, XRD); and catalyst synthesis characterization (FT-IR, ^{1}H NMR, UV−vis) (PDF)

https://doi.org/10.1021/acsanm.3c01591
ACS Appl. Nano Mater. 2023, 6, 10626−10635

AUTHOR INFORMATION

Corresponding Authors

Umit Isci − *Department of Metallurgical & Materials Engineering, Marmara University, Faculty of Technology, 34722 Istanbul, Türkiye*; Email: umit.isci@marmara.edu.tr

Negar Naghavi − *Institut Photovoltaïque d'Île-de-France (IPVF), CNRS, UMR 9006, 91120 Palaiseau, France*; orcid.org/0000-0002-6045-5096; Email: negar.naghavi@chimieparistech.psl.eu

Marc Robert − *Laboratoire d'Electrochimie Moléculaire, Université Paris Cité, CNRS, F-75006 Paris, France; Institut Universitaire de France (IUF), F-75005 Paris, France*; orcid.org/0000-0001-7042-4106; Email: robert@u-paris.fr

Authors

Julian Guerrero − *Laboratoire d'Electrochimie Moléculaire, Université Paris Cité, CNRS, F-75006 Paris, France; Institut Photovoltaïque d'Île-de-France (IPVF), CNRS, UMR 9006, 91120 Palaiseau, France*

Nathanaelle Schneider − *Institut Photovoltaïque d'Île-de-France (IPVF), CNRS, UMR 9006, 91120 Palaiseau, France*

Fabienne Dumoulin − *Biomedical Engineering Department, Acıbadem Mehmet Ali Aydınlar University, Faculty of Engineering and Natural Sciences, 34752 Ataşehir, Istanbul, Türkiye*; orcid.org/0000-0002-0388-8338

Daniel Lincot − *Institut Photovoltaïque d'Île-de-France (IPVF), CNRS, UMR 9006, 91120 Palaiseau, France*

Complete contact information is available at: https://pubs.acs.org/10.1021/acsanm.3c01591

Author Contributions

The manuscript was written through contributions of all authors. All authors have given approval to the final version of the manuscript.

Notes

The authors declare no competing financial interest.

ACKNOWLEDGMENTS

The authors are very grateful for the financial support from the CNRS through the 80|Prime program. M.R. acknowledges the Institut Universitaire de France (IUF) for partial financial support.

REFERENCES

(1) Kayan, A. Inorganic-Organic Hybrid Materials and Their Adsorbent Properties. *Adv. Compos. Mater.* **2019**, *2*, 34−45.

(2) Ananikov, V. P. Organic−Inorganic Hybrid Nanomaterials. *Nanomaterials* **2019**, *9*, 1197.

(3) Chongdar, S.; Bhattacharjee, S.; Bhanja, P.; Bhaumik, A. Porous Organic−Inorganic Hybrid Materials for Catalysis, Energy and Environmental Applications. *Chem. Commun.* **2022**, *58*, 3429−3460.

(4) Sun, Y.; Wang, F.; Fu, Y.; Chen, C.; Wang, X.; Xiao, Z.; Liu, Y.; Xu, J.; Li, B.; Wang, L. Two New Inorganic−Organic Hybrid Zinc Phosphites and Their Derived ZnO/ZnS Heterostructure for Efficient Photocatalytic Hydrogen Production. *RSC Adv.* **2020**, *10*, 812−817.

(5) Li, M.; Garg, S.; Chang, X.; Ge, L.; Li, L.; Konarova, M.; Rufford, T. E.; Rudolph, V.; Wang, G. Toward Excellence of Transition Metal-Based Catalysts for CO_2 Electrochemical Reduction: An Overview of Strategies and Rationales. *Small Methods* **2020**, *4*, No. 2000033.

(6) Li, T.-T.; Mei, Y.; Li, H.; Qian, J.; Wu, M.; Zheng, Y.-Q. Highly Selective and Active Electrochemical Reduction of CO_2 to CO on a Polymeric Co(II) Phthalocyanine@Graphitic Carbon Nitride Nanosheet−Carbon Nanotube Composite. *Inorg. Chem.* **2020**, *59*, 14184−14192.

(7) Kinzel, N. W.; Werlé, C.; Leitner, W. Transition Metal Complexes as Catalysts for the Electroconversion of CO_2: An Organometallic Perspective. *Angew. Chem., Int. Ed.* **2021**, *60*, 11628−11686.

(8) Leung, C.-F.; Ho, P.-Y. Molecular Catalysis for Utilizing CO_2 in Fuel Electro-Generation and in Chemical Feedstock. *Catalysts* **2019**, *9*, 760.

(9) Dalle, K. E.; Warnan, J.; Leung, J. J.; Reuillard, B.; Karmel, I. S.; Reisner, E. Electro- and Solar-Driven Fuel Synthesis with First Row Transition Metal Complexes. *Chem. Rev.* **2019**, *119*, 2752−2875.

(10) Wang, M.; Torbensen, K.; Salvatore, D.; Ren, S.; Joulié, D.; Dumoulin, F.; Mendoza, D.; Lassalle-Kaiser, B.; Işci, U.; Berlinguette, C. P.; Robert, M. CO_2 Electrochemical Catalytic Reduction with a Highly Active Cobalt Phthalocyanine. *Nat. Commun.* **2019**, *10*, No. 3602.

(11) Ren, S.; Joulié, D.; Salvatore, D.; Torbensen, K.; Wang, M.; Robert, M.; Berlinguette, C. P. Molecular Electrocatalysts Can Mediate Fast, Selective CO_2 Reduction in a Flow Cell. *Science* **2019**, *365*, 367−369.

(12) Cheng, D.; Zhao, Z.-J.; Zhang, G.; Yang, P.; Li, L.; Gao, H.; Liu, S.; Chang, X.; Chen, S.; Wang, T.; Ozin, G. A.; Liu, Z.; Gong, J. The Nature of Active Sites for Carbon Dioxide Electroreduction over Oxide-Derived Copper Catalysts. *Nat. Commun.* **2021**, *12*, No. 395.

(13) Pander, J. E.; Ren, D.; Huang, Y.; Loo, N. W. X.; Hong, S. H. L.; Yeo, B. S. Understanding the Heterogeneous Electrocatalytic Reduction of Carbon Dioxide on Oxide-Derived Catalysts. *ChemElectroChem* **2018**, *5*, 219−237.

(14) Dattila, F.; García-Muelas, R.; López, N. Active and Selective Ensembles in Oxide-Derived Copper Catalysts for CO_2 Reduction. *ACS Energy Lett.* **2020**, *5*, 3176−3184.

(15) Verdaguer-Casadevall, A.; Li, C. W.; Johansson, T. P.; Scott, S. B.; McKeown, J. T.; Kumar, M.; Stephens, I. E. L.; Kanan, M. W.; Chorkendorff, I. Probing the Active Surface Sites for CO Reduction on Oxide-Derived Copper Electrocatalysts. *J. Am. Chem. Soc.* **2015**, *137*, 9808−9811.

(16) Kostecki, R.; Augustynski, J. Electrochemical Reduction of CO_2 at an Activated Silver Electrode. *Ber. Bunsenges. Phys. Chem.* **1994**, *98*, 1510−1515.

(17) Ma, M.; Trześniewski, B. J.; Xie, J.; Smith, W. A. Selective and Efficient Reduction of Carbon Dioxide to Carbon Monoxide on Oxide-Derived Nanostructured Silver Electrocatalysts. *Angew. Chem., Int. Ed.* **2016**, *55*, 9748−9752.

(18) Bi, Q.; Huang, X.; Yin, G.; Chen, T.; Du, X.; Cai, J.; Xu, J.; Liu, Z.; Han, Y.; Huang, F. Cooperative Catalysis of Nickel and Nickel Oxide for Efficient Reduction of CO2 to CH4. *ChemCatChem* **2019**, *11*, 1295−1302.

(19) Wang, Z.; Fan, J.; Cheng, B.; Yu, J.; Xu, J. Nickel-Based Cocatalysts for Photocatalysis: Hydrogen Evolution, Overall Water Splitting and CO_2 Reduction. *Mater. Today Phys.* **2020**, *15*, No. 100279.

(20) Dey, G. R.; Belapurkar, A. D.; Kishore, K. Photo-Catalytic Reduction of Carbon Dioxide to Methane Using TiO_2 as Suspension in Water. *J. Photochem. Photobiol., A* **2004**, *163*, 503−508.

(21) Shehzad, N.; Tahir, M.; Johari, K.; Murugesan, T.; Hussain, M. A Critical Review on TiO_2 Based Photocatalytic CO_2 Reduction System: Strategies to Improve Efficiency. *J. CO_2 Util.* **2018**, *26*, 98−122.

(22) Jin, L.; Shaaban, E.; Bamonte, S.; Cintron, D.; Shuster, S.; Zhang, L.; Li, G.; He, J. Surface Basicity of Metal@TiO_2 to Enhance Photocatalytic Efficiency for CO_2 Reduction. *ACS Appl. Mater. Interfaces* **2021**, *13*, 38595−38603.

(23) Djurišić, A.; Leung, Y. H. Optical Properties of ZnO Nanostructures. *Small* **2006**, *2*, 944−961.

(24) Rezaie, M. N.; Mohammadnejad, S.; Ahadzadeh, S. Hybrid Inorganic-Organic Light-Emitting Heterostructure Devices Based on ZnO. *Opt. Laser Technol.* **2021**, *138*, No. 106896.

(25) Kao, M.-C.; Chen, H.-Z.; Young, S.-L.; Lin, C.-C.; Kung, C.-Y. Structure and Photovoltaic Properties of ZnO Nanowire for Dye-Sensitized Solar Cells. *Nanoscale Res. Lett.* **2012**, *7*, 260.
(26) Manor, A.; Katz, E. A.; Tromholt, T.; Krebs, F. C. Enhancing Functionality of ZnO Hole Blocking Layer in Organic Photovoltaics. *Sol. Energy Mater. Sol. Cells* **2012**, *98*, 491−493.
(27) Sharma, A.; Franklin, J. B.; Singh, B.; Andersson, G. G.; Lewis, D. A. Electronic and Chemical Properties of ZnO in Inverted Organic Photovoltaic Devices. *Org. Electron.* **2015**, *24*, 131−136.
(28) Luo, W.; Zhang, Q.; Zhang, J.; Moioli, E.; Zhao, K.; Züttel, A. Electrochemical Reconstruction of ZnO for Selective Reduction of CO_2 to CO. *Appl. Catal., B* **2020**, *273*, No. 119060.
(29) Han, K.; Ngene, P.; Jongh, P. Structure Dependent Product Selectivity for CO_2 Electroreduction on ZnO Derived Catalysts. *ChemCatChem* **2021**, *13*, 1998−2004.
(30) Raula, M.; Rashid, Md. H.; Paira, T. K.; Dinda, E.; Mandal, T. K. Ascorbate-Assisted Growth of Hierarchical ZnO Nanostructures: Sphere, Spindle, and Flower and Their Catalytic Properties. *Langmuir* **2010**, *26*, 8769−8782.
(31) Kumar, S.; Kumar, A.; Kumar, A.; Krishnan, V. Nanoscale Zinc Oxide Based Heterojunctions as Visible Light Active Photocatalysts for Hydrogen Energy and Environmental Remediation. *Catal. Rev. Sci. Eng.* **2020**, *62*, 346−405.
(32) Jiang, X.; Cai, F.; Gao, D.; Dong, J.; Miao, S.; Wang, G.; Bao, X. Electrocatalytic Reduction of Carbon Dioxide over Reduced Nanoporous Zinc Oxide. *Electrochem. Commun.* **2016**, *68*, 67−70.
(33) Jehl, Z.; Rousset, J.; Donsanti, F.; Renou, G.; Naghavi, N.; Lincot, D. Electrodeposition of ZnO Nanorod Arrays on ZnO Substrate with Tunable Orientation and Optical Properties. *Nanotechnology* **2010**, *21*, No. 395603.
(34) Pauporté, T.; Bataille, G.; Joulaud, L.; Vermersch, F. J. Well-Aligned ZnO Nanowire Arrays Prepared by Seed-Layer-Free Electrodeposition and Their Cassie−Wenzel Transition after Hydrophobization. *J. Phys. Chem. C* **2010**, *114*, 194−202.
(35) Choi, K.-S.; Chang, S.-P. Effect of Structure Morphologies on Hydrogen Gas Sensing by ZnO Nanotubes. *Mater. Lett.* **2018**, *230*, 48−52.
(36) Pelicano, C. M.; Yanagi, H. Enhanced Charge Transport in Al-Doped ZnO Nanotubes Designed *via* Simultaneous Etching and Al Doping of H_2O-Oxidized ZnO Nanorods for Solar Cell Applications. *J. Mater. Chem. C* **2019**, *7*, 4653−4661.
(37) Kim, K.; Choi, P. g.; Itoh, T.; Masuda, Y. Atomic Step Formation on Porous ZnO Nanobelts: Remarkable Promotion of Acetone Gas Detection up to the Parts per Trillion Level. *J. Mater. Chem. A* **2022**, *10*, 13839−13847.
(38) Hong, M.; Meng, J.; Yu, H.; Du, J.; Ou, Y.; Liao, Q.; Kang, Z.; Zhang, Z.; Zhang, Y. Ultra-Stable ZnO Nanobelts in Electrochemical Environments. *Mater. Chem. Front.* **2021**, *5*, 430−437.
(39) Taunk, P. B.; Das, R.; Bisen, D. P.; Tamrakar, R. K.; Rathor, N. Synthesis and Optical Properties of Chemical Bath Deposited ZnO Thin Film Karbala. *Int. J. Mod. Sci.* **2015**, *1*, 159−165.
(40) Sánchez-Martín, S.; Olaizola, S. M.; Castaño, E.; Urionabarrenetxea, E.; Mandayo, G. G.; Ayerdi, I. Study of Deposition Parameters and Growth Kinetics of ZnO Deposited by Aerosol Assisted Chemical Vapor Deposition. *RSC Adv.* **2021**, *11*, 18493−18499.
(41) Nozik, A. J. Photoelectrochemical cells. *Philos. Trans. R. Soc., A* **1980**, *295*, 453−470.
(42) Peulon, S.; Lincot, D. Cathodic Electrodeposition from Aqueous Solution of Dense or Open-Structured Zinc Oxide Films. *Adv. Mater.* **1996**, *8*, 166−170.
(43) Izaki, M.; Omi, T. Transparent Zinc Oxide Films Prepared by Electrochemical Reaction. *Appl. Phys. Lett.* **1996**, *68*, 2439−2440.
(44) Yoshida, T.; Minoura, H. Electrochemical Self-Assembly of Dye-Modified Zinc Oxide Thin Films. *Adv. Mater.* **2000**, *12*, 1219−1222.
(45) Haller, S.; Suguira, T.; Lincot, D.; Yoshida, T. Design of a Hierarchical Structure of ZnO by Electrochemistry for ZnO-Based Dye-Sensitized Solar Cells: Design of a Hierarchical Structure of ZnO by Electrochemistry. *Phys. Status Solidi A* **2010**, *207*, 2252−2257.
(46) Yoshida, T.; Tochimoto, M.; Schlettwein, D.; Wöhrle, D.; Sugiura, T.; Minoura, H. Self-Assembly of Zinc Oxide Thin Films Modified with Tetrasulfonated Metallophthalocyanines by One-Step Electrodeposition. *Chem. Mater.* **1999**, *11*, 2657−2667.
(47) Pauporté, T.; Yoshida, T.; Cortès, R.; Froment, M.; Lincot, D. Electrochemical Growth of Epitaxial Eosin/ZnO Hybrid Films. *J. Phys. Chem. B* **2003**, *107*, 10077−10082.
(48) Pauporté, T.; Bedioui, F.; Lincot, D. Nanostructured Zinc Oxide−Chromophore Hybrid Films with Multicolored Electrochromic Properties. *J. Mater. Chem.* **2005**, *15*, 1552−1559.
(49) Yang, H.; Wang, X.; Hu, Q.; Chai, X.; Ren, X.; Zhang, Q.; Liu, J.; He, C. Recent Progress in Self-Supported Catalysts for CO_2 Electrochemical Reduction. *Small Methods* **2020**, *4*, No. 1900826.
(50) Basnet, P.; Samanta, D.; Inakhunbi Chanu, T.; Mukherjee, J.; Chatterjee, S. Assessment of Synthesis Approaches for Tuning the Photocatalytic Property of ZnO Nanoparticles. *SN Appl. Sci.* **2019**, *1*, 633.
(51) Höchst, H.; Goldmann, A.; Hüfner, S.; Malter, H. X-Ray Photoelectron Valence Band Studies on Phthalocyanine Compounds. *Phys. Status Solidi B* **1976**, *76*, 559−586.
(52) Hellgren, N.; Guo, J.; Luo, Y.; Såthe, C.; Agui, A.; Kashtanov, S.; Nordgren, J.; Ågren, H.; Sundgren, J.-E. Electronic Structure of Carbon Nitride Thin Films Studied by X-Ray Spectroscopy Techniques. *Thin Solid Films* **2005**, *471*, 19−34.
(53) Neelgund, G. M.; Oki, A. Cobalt Phthalocyanine-Sensitized Graphene−ZnO Composite: An Efficient Near-Infrared-Active Photothermal Agent. *ACS Omega* **2019**, *4*, 5696−5704.
(54) Luo, W.; Zhang, Q.; Zhang, J.; Moioli, E.; Zhao, K.; Züttel, A. Electrochemical Reconstruction of ZnO for Selective Reduction of CO_2 to CO. *Appl. Catal., B* **2020**, *273*, No. 119060.
(55) Geng, Z.; Kong, X.; Chen, W.; Su, H.; Liu, Y.; Cai, F.; Wang, G.; Zeng, J. Oxygen Vacancies in ZnO Nanosheets Enhance CO2 Electrochemical Reduction to CO. *Angew. Chem., Int. Ed.* **2018**, *130*, 6162−6167.
(56) Xiang, Q.; Li, F.; Wang, J.; Chen, W.; Miao, Q.; Zhang, Q.; Tao, P.; Song, C.; Shang, W.; Zhu, H.; Deng, T.; Wu, J. Heterostructure of ZnO Nanosheets/Zn with a Highly Enhanced Edge Surface for Efficient CO_2 Electrochemical Reduction to CO. *ACS Appl. Mater. Interfaces* **2021**, *13*, 10837−10844.
(57) Liu, K.; Wang, J.; Shi, M.; Yan, J.; Jiang, Q. Simultaneous Achieving of High Faradaic Efficiency and CO Partial Current Density for CO_2 Reduction via Robust, Noble-Metal-Free Zn Nanosheets with Favorable Adsorption Energy. *Adv. Energy Mater.* **2019**, *9*, No. 1900276.
(58) Zong, X.; Jin, Y.; Li, Y.; Zhang, X.; Zhang, S.; Xie, H.; Zhang, J.; Xiong, Y. Morphology-Controllable ZnO Catalysts Enriched with Oxygen-Vacancies for Boosting CO_2 Electroreduction to CO. *J. CO_2 Util.* **2022**, *61*, No. 102051.
(59) Zhang, X.; Wu, Z.; Zhang, X.; Li, L.; Li, Y.; Xu, H.; Li, X.; Yu, X.; Zhang, Z.; Liang, Y.; Wang, H. Highly Selective and Active CO_2 Reduction Electrocatalysts Based on Cobalt Phthalocyanine/Carbon Nanotube Hybrid Structures. *Nat. Commun.* **2017**, *8*, No. 14675.
(60) Mai, N. T.; Thuy, T. T.; Mott, D. M.; Maenosono, S. Chemical Synthesis of Blue-Emitting Metallic Zinc Nano-Hexagons. *CrystEngComm* **2013**, *15*, 6606.
(61) Le Tulzo, H.; Schneider, N.; Lincot, D.; Patriarche, G.; Donsanti, F. Impact of the Sequence of Precursor Introduction on the Growth and Properties of Atomic Layer Deposited Al-Doped ZnO Films. *J. Vac. Sci. Technol., A* **2018**, *36*, No. 041502.
(62) König, M.; Vaes, J.; Klemm, E.; Pant, D. Solvents and Supporting Electrolytes in the Electrocatalytic Reduction of CO_2. *iScience* **2019**, *19*, 135−160.
(63) Pati, P. B.; Wang, R.; Boutin, E.; Diring, S.; Jobic, S.; Barreau, N.; Odobel, F.; Robert, M. Photocathode Functionalized with a Molecular Cobalt Catalyst for Selective Carbon Dioxide Reduction in Water. *Nat. Commun.* **2020**, *11*, No. 3499.

https://doi.org/10.1021/acsanm.3c01591
ACS Appl. Nano Mater. 2023, 6, 10626−10635